

# Exciton Mott Transition in Two-Dimensional Semiconductors

Yiling Yu<sup>1</sup>, Guoqing Li<sup>1</sup>, Linyou Cao<sup>1,2,3\*</sup>

<sup>1</sup>Department of Materials Science and Engineering, North Carolina State University, Raleigh, North Carolina, 27695, United States; <sup>2</sup>Department of Physics, North Carolina State University, Raleigh, North Carolina, 27695, United States; <sup>3</sup>Department of Electrical and Computer Engineering, North Carolina State University, Raleigh, North Carolina, 27695, United States

## Abstract

The many-body interaction of quantum particles or quasi-particles underlies major modern scientific discoveries and technological breakthroughs, such as superconductivity, Bose-Einstein condensation, and quantum computing. Excitons, a non-equilibrium quantum quasi-particle, offer a tantalizing prospect of externally controlling quantum systems due to the non-equilibrium nature, but the fundamental understanding of exciton many-body interaction is limited. Here we provide a new comprehensive physics scheme for exciton Mott transition (EMT), a key manifestation of exciton many-body interaction as evidenced by exciton ionization into electron-hole plasma (EHP). We clarify numerous long-standing controversies (the continuousness and criteria of EMT), address unanswered key questions (quantifying exciton-EHP equilibrium and the correlation of EHP charge density-emission), and discover unexplored physics (EHP charges clustering as nanoscale complex rather than existing individually). These results form a base to facilitate the studies of exciton many-body interaction, and lays down a cornerstone for using the interaction in quantum science/technology and the development of advanced optoelectronic devices.

\* Correspondence should be addressed to: [linyoucao@gmail.com](mailto:linyoucao@gmail.com)

The many body interaction of quantum particles or quasi-particles such as electrons, phonons, excitons, and spins is one of the most exciting topical research areas of modern materials science, as it underlies many major modern scientific discoveries and technological breakthroughs, such as superconductivity<sup>1</sup>, Bose-Einstein condensation<sup>2</sup>, topological insulator<sup>3</sup>, quantum entanglement<sup>4</sup>, and quantum computing<sup>5</sup>. Excitons, which consist of pair-wise electrons and holes bound by Coulomb attraction and are foundation of all optoelectronic devices, present a type of non-equilibrium quantum quasi-particles that are particularly intriguing.<sup>6,7</sup> Unlike other basic particles or quasi-particles such as electrons or phonons, which are inherent to matters, excitons do not naturally exist unless the presence of external excitation, either optical or electrical. This feature offers opportunities to externally control quantum many-body interactions that are difficult or not possible with other particles.

The nature of exciton many-body interaction may be manifested by the phase transition of excitons.<sup>8-13</sup> Generally, excitons at a low density behave like free gas molecules due to little exciton-exciton interaction, referred as free excitons (FEs). With the density increasing, the exciton many-body interaction becomes prominent to screen the pair-wise Coulomb attraction, which may enable exciton Mott transition (EMT) with excitons ionized into a plasma of unbound electrons and holes, *i.e.* electron-hole plasma (EHP).<sup>14-18</sup> At the highest density, even stronger exciton many-body interaction can cause EHP or excitons to undergo a gas-liquid transition into a liquid-like state, *i.e.* electron-hole liquid (EHL).<sup>9,11,16,19-21</sup> However, the fundamental understanding of exciton many-body interaction is very limited due to many challenges in studying exciton phase transitions. For instance, the key challenge for the studies of EMT lies in the difficulty to deterministically distinguish the signal from the various co-existing excitonic species, including free excitons, trions, bi-excitons, and EHP.<sup>14,16,22</sup> The emission of these species in

conventional semiconductors are very close with energy difference usually less than 5 meV and thus difficult to separate.<sup>16,22</sup> Additionally, the intense external excitation (such as laser) required to enable EMT may induce inhomogeneity inside the conventional semiconductors due to the materials' non-trivial dimension, which can broaden the spectral distribution of emission and makes the separation more difficult.

Two-dimensional (2D) semiconductors provide an ideal platform for the studies of EMT, as its extraordinary binding energy enables larger energy separation between different excitonic species and the atomically thin dimension minimizes laser-induced inhomogeneity. Indeed, EMT have been recently reported at 2D semiconductors,<sup>15,17,18</sup> but no satisfactory understanding for the fundamentals of EMT is provided. Here we establish a new physics scheme for EMT by taking advantage of 2D semiconductors. Fig.1 shows the evolution of PL's spatial and spectral features collected from suspended monolayer MoS<sub>2</sub> as a function of incident power densities. The result indicates the presence of two turnpoints (critical incident powers) at which the PL substantially changes, one at the incidence around 8.0 kW/cm<sup>2</sup> and the other at around 20.0 kW/cm<sup>2</sup>. The turnpoint at 20.0 kW/cm<sup>2</sup>, which can be correlated to the gas-liquid phase transition according to our previous studies,<sup>11</sup> features a substantial shrinking of the luminescence area, a sharp increase in the PL intensity, and a tendency of the PL width and peak position turning to be power independent. In this study, we focus on the turnpoint at 8.0 kW/cm<sup>2</sup> that can be correlated to EMT according to previous studies<sup>11</sup>. It features an expansion of the luminescence area, a change of the PL intensity from power-dependent to power-independent, and a larger broadening of the PL spectral width with increase of the incident power.

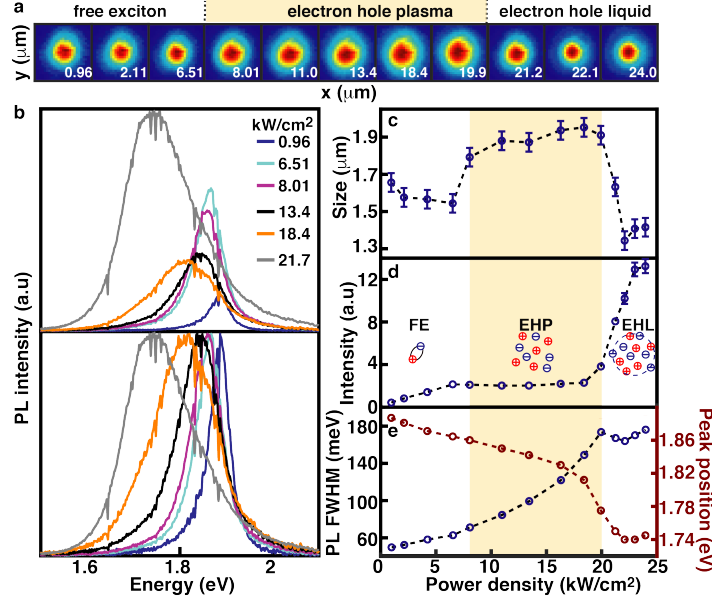


**Figure 1. Experimental evidence for exciton phase transition in suspended monolayer MoS<sub>2</sub>.** (a) Spatial PL imaging collected from a suspended CVD-grown monolayer MoS<sub>2</sub> flake (suspended area is in radius of 4.0 μm, see optical image in Fig. S1) under the incidence of a focused 532 nm laser (in radius of 1.10 μm) with different incident power densities. The white number indicates the incident power density with a unit of kW/cm<sup>2</sup>. (b) As-measured (top panel) and normalized (bottom panel) PL spectra collected from the luminescence center of monolayer MoS<sub>2</sub> under different incident power densities. (c) The size of the luminescence area (spatial full width at half magnitude), (d) the PL intensity, (e) the PL's peak position (red) and spectral full width half magnitude (FWHM, blue) as a function of the incident power density, which are extracted from the results in (a) and (b). The exciton phase transition is evidenced by the substantial changes in PL at two turnpoints, one at 8.0 kW/cm<sup>2</sup> resulting from exciton Mott transition and the other at 20.0 kW/cm<sup>2</sup> from exciton gas-liquid phase transition. The areas with different colors in (a) and (c-e) indicate the different physical states of excitons, including free excitons (FEs), electron-hole plasma (EHP), and electron-hole liquid (EHL). Error bars are not plotted for the datapoints whose measurement error is smaller than the size of the dot.

### Evidence for exciton Mott transition and its continuousness

To better support the correlation of the turnpoint at 8.0 kW/cm<sup>2</sup> to EMT, we first exclude the possible defect generation and temperature increase induced by the incident laser being the reason for the change of PL at 8.0 kW/cm<sup>2</sup>. The exclusion of defect effect is evidenced by reversible change of PL when surveying the incident power back and forth across 8.0 kW/cm<sup>2</sup>, as

the effect of defects would be permanent (Fig. S2). It is also supported by high similarity between the Raman spectra collected from the monolayer before and after the measurement (Fig. S3). Additionally, the photothermally induced temperature increase may account for the broadening and redshift of the PL at  $< 8.0 \text{ kW/cm}^2$ , but not at  $> 8.0 \text{ kW/cm}^2$  (Fig. 2a), which indicates the temperature increase does not play a major role in the PL change above the turnpoint.

In principle, the increase of incident power could also induce the formation of trions or biexcitons that would cause PL to broaden and redshift,<sup>23,24</sup> but we can also exclude trions or biexcitons being the major reason for the turnpoint at  $8.0 \text{ kW/cm}^2$ . The exclusion is first intuitively supported by the power-independent PL intensity under the incident powers beyond the turnpoint, which does not match the exponential power-dependence expected for trion or biexciton emission<sup>25</sup> and indicates that trions or biexcitons, if any, do not play a major role in the PL. The exclusion is also supported by quantitative analysis of the PL spectra. Unlike the PL spectra at low incident powers, which features a sharp peak from neutral *A* exciton of monolayer MoS<sub>2</sub> (Fig. 2b),<sup>26,27</sup> the PL spectra beyond the turnpoint often involves a main peak accompanied by a weak shoulder peak (Fig. 2b). Guided by the visible shoulder peaks, we can fit the PL spectra in the range of  $8.0\text{-}20.0 \text{ kW/cm}^2$  to combination of a narrow peak at  $1.86\text{-}1.87 \text{ eV}$  (peak 1) and a broad peak at lower energies (peak 2) (Fig. 2c). The narrow peak at  $1.86\text{-}1.87 \text{ eV}$  can be readily ascribed to exciton emission (Fig. 2b). The broad emission shows distinct power dependence from the exciton emission (Fig. 2d-f). It shows intensity increase, substantial redshift, and broadening with the incident power increasing, while the exciton emission shows decrease in intensity and negligible change in peak position and spectral width. The distinct power dependence indicates that trions or bi-excitons are not the major source of the broad emission, because the emission of trions or biexcitons is expected to be pinned with the exciton emission as reported previously,<sup>23,25</sup> including

a constant energy difference in emission peak position and a same direction in the change of emission intensity with the incident power.

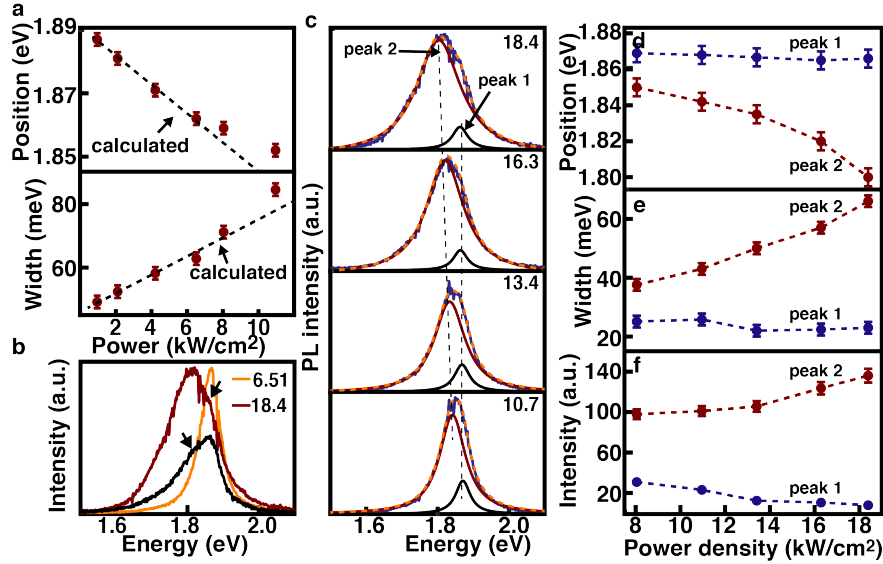


**Figure 2. Exclusion of temperature increase and trions/bi-excitons for the turnpoint of 8.0 kW/cm<sup>2</sup>.** (a) measured (dots) and calculated (dashed line) peak position, and (b) measured (dots) and calculated (dashed line) spectra width as a function of incident power. The calculation is on basis of temperature increase induced by the photothermal effect of incident laser. The temperature increase is calculated following the method reported previously<sup>28</sup> and the given calculation result is obtained by multiplying the temperature increase with a temperature-dependent redshift (0.317 meV/K) and broadening coefficient (0.22 meV/K) reported in.<sup>11</sup> The result indicates that the laser-induced temperature increase may account for the broadening and redshift of the PL at < 8.0 kW/cm<sup>2</sup>, but cannot explain the result at > 8.0 kW/cm<sup>2</sup> (c) Representative PL spectra collected from the monolayer under the incident power below (orange) and beyond (red and black) 8.0 kW/cm<sup>2</sup>. The arrows point towards shoulder peaks in the PL spectra. (d) PL spectra collected with different incident powers beyond 8.0 kW/cm<sup>2</sup> (as indicated by the given number with a unit of kW/cm<sup>2</sup>) and corresponding fitting. The spectra can be fitted as combination of one narrow peak at 1.86-1.87 eV (peak 1) and another broader one at lower energies (peak 2). The dashed lines illustrate the shift of the positions of peak 1 and peak 2. (d) Intensity, (e) peak position, and (f) spectral width of the fitted peaks (blue, peak 1; red, peak 2) as a function of the incident power.

Indeed, all the power-dependent features of the PL as shown in Fig. 2d-f can be nicely explained by correlating the broad emission to EHP and the turn at 8.0 kW/cm<sup>2</sup> to EMT. EHP results from exciton ionization due to the screening of pair-wise Coulomb attraction with the presence of a large density of charge carriers. It features a broad emission at energies lower than exciton emission.<sup>8,11,15,17,29</sup> With the incident power increasing, the pair-wise Coulomb attraction

can be further screened, leading to an increase in exciton ionization and charge density of the EHP. This may account for the observed intensity increase, redshift, and broadening of the broad emission (Fig. 2d-f), because EHP emission redshifts and broadens with the charge density increasing.<sup>8,11,15,17,22</sup> The increase of Coulomb screening can also lead to a decrease in exciton binding energy and exciton emission efficiency<sup>30</sup> (Fig. 2f). The opposite effects of the Coulomb screening on the EHP emission and exciton emission may offset each other, giving rise to the observed power independence of the overall emission intensity (Fig. 1d). Additionally, EHP can account for the negligible redshift and broadening of the exciton emission with increase of the incident power at  $> 8.0 \text{ kW/cm}^2$  (Fig. 2e), which is in stark contrast with the substantial thermally induced redshift and broadening at low incident powers (Fig. 2a). The unbound charge carriers in EHP can provide much stronger Coulomb screening effect than excitons.<sup>15,31</sup> The Coulomb screening can affect the exciton peak position via two pathways, reducing exciton binding energy and inducing bandgap renormalization,<sup>32-34</sup> and these two effects may collectively offset the thermally induced redshift. The unbound charge carriers may also provide screening for the scattering of excitons with phonons,<sup>35</sup> the major mechanism for thermally induced broadening in emission, and gives rise to the negligible broadening of exciton emission with incident power increasing.

Significantly, the experimental result clarifies a long-standing controversy about EMT, whether it is continuous or abrupt. The observed continuous evolution of the EHP emission with the incident power (Fig. 2d-f) indicates that the EMT is a continuous process. As illustrated in Fig. 3a, the EMT starts at the incident power of around  $8.0 \text{ kW/cm}^2$ , continuously evolves with further increase of the incident power, and terminates by merging into the gas-liquid phase transition at around  $20.0 \text{ kW/cm}^2$ .

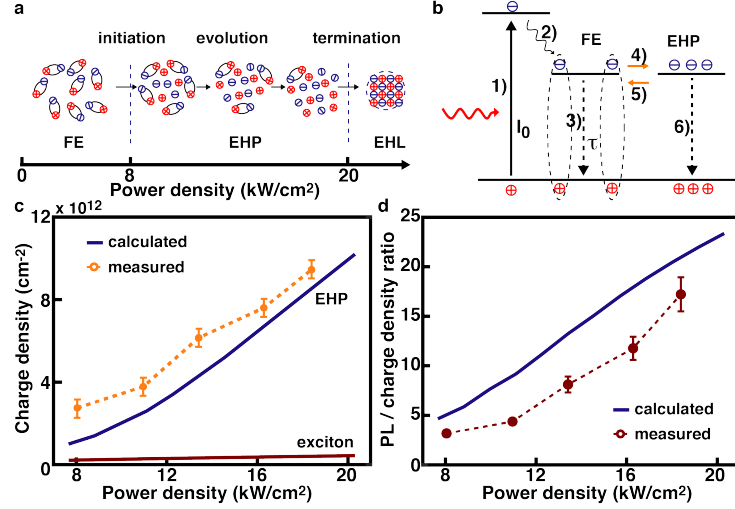


**Figure 3. Quantification of charge densities in EHP and co-existing excitons.** (a) Schematic illustration for the continuous exciton Mott transition as a function of incident power, starting at 8.0 kW/cm<sup>2</sup>, evolving with increase in incident power, and terminating by merging into the gas-liquid phase transition at 20.0 kW/cm<sup>2</sup>. (b) Schematic illustration for the charge dynamics involved in exciton Mott transition. The process involves 1) photogeneration of charge carriers, 2) relaxing to band edges, 3) exciton recombination, 4) exciton ionization into EHP, 5) de-ionization of EHP to excitons, and 6) EHP recombination. (c) Charge densities in EHP (blue) and co-existing excitons (red) as a function of incident power. The charge densities estimated on basis of the measured spectral width of EHP emission as shown in Fig.2e are also plotted (orange dots). (d) The calculated ratio of charge densities in the EHP and co-existing excitons (blue line) and the measured intensity ratio of EHP and exciton emission (red dots) as a function of incident power.

### Quantification of the charge density distribution in EHP and excitons

We develop new understanding to quantify the distribution of charge carriers among the EHP and co-existing excitons, which has been elusive due to the difficulty in deterministically distinguishing the signals from different excitonic species in previous studies.<sup>16,22</sup> According to our new understanding, the dynamics of excitons and EHP can be considered being reasonably decoupled in time and Saha equation governs the equilibrium between EHP and excitons. As illustrated in Fig. 3b, excitons are generated upon photoexcitation followed by a fast thermalization process relaxing to the band edges. After that, the excitons decay through linear and nonlinear recombination as well as ionization (to form EHP). The resulting EHP decays via recombination and a de-ionization process (back to excitons). This complicated dynamic process can be



reasonably simplified on basis of our experimental observation<sup>8,36</sup> and results in references<sup>22,37-39</sup>. We previously demonstrated that the lifetime of excitons in suspended monolayer MoS<sub>2</sub> is around 1 ns.<sup>36</sup> We also demonstrated that, upon the incidence of laser power in the EHP regime, excitons are formed first followed by the formation of EHP and the process of exciton ionization to form EHP is at the scale of 100-300 ns.<sup>8</sup> Additionally, it has been well documented in references that the formation of excitons is fast but the process of forming stable EHP phase or EHL is slower, which could take time as long as 150 ns.<sup>22,37-39</sup> Therefore, the dynamics of excitons and EHP can be considered being decoupled in time. The system first reaches a steady state of excitons, and then the steady-state excitons undergo a slow ionization process to gradually build up EHP until an equilibrium between the excitons and EHP is reached, during which the steady-state exciton density does not change much. With this simplification, we can evaluate the steady-state exciton density without considering the ionization process as what we did elsewhere (see S1 for details).

<sup>40</sup> On basis of the calculated exciton density, we can then estimate the charge density of EHP with Saha equation (see S2 for details), which has been extensively used to describe plasma ionization under thermodynamic equilibrium.<sup>41</sup> The calculation results (Fig. 3c) indicate that the charge density of the EHP rapidly increases by 10 folds from  $1.0 \times 10^{12} \text{ cm}^{-2}$  to  $1.0 \times 10^{13} \text{ cm}^{-2}$  in the incident power range of 8.0 - 20.0 kW/cm<sup>2</sup>, while the density of the co-existing excitons only increases by 2 times from  $\sim 2.0 \times 10^{11} \text{ cm}^{-2}$  to  $\sim 4.0 \times 10^{11} \text{ cm}^{-2}$ .

We assume negligible change in the steady-state exciton density during the slow process of forming EHP, in which the charge built-up in EHP essentially originates from the continuous laser incidence but is mediated by excitons, very similar to the way of energy built-up in coupled optical systems.<sup>42</sup> As a matter of fact, the presence of EHP could affect the dynamics of excitons in multiple ways, such as Coulomb screening and charge-charge scattering. However, the

calculated charge densities are reasonably consistent with well-accepted common sense, our experimental observation, and theoretical prediction. This indicates the reasonableness of the assumption, which could be due to the mutual cancelation of the multiple effects of EHP on the exciton density. First, the ratio of the calculated charge density for the onset and termination (merging into the gas-liquid phase) of the EMT stage is 10. This is consistent with the widely accepted common sense that the critical charge density for the onset of EMT is usually one order of magnitude lower than that for the gas-liquid phase transition.<sup>16,22</sup> Second, the calculation result matches our experimental observation. The calculated charge density in EHP is reasonably consistent with the charge density derived from the spectral width of the measured EHP emission that is extracted from Fig. 2e (orange dots in Fig. 3c). As discussed later in Fig. 5, the charge density of EHP can be found out from the spectral width of the EHP emission, as the EHP spectral width is dictated by the Fermi energy of the unbound charge carriers and the spectral width of the co-existing exciton emission. Additionally, the ratio of the calculated charge density in EHP and excitons reasonably matches the ratio of the measured PL intensity from EHP and co-existing excitons (red dots in Fig. 3d). This consistence suggests that EHP has a similar radiative lifetime as the co-existing excitons, which is reasonable as previous studies on EHP demonstrates that the relative charge densities of co-existing excitonic species can be correlated to the ratio of corresponding PL intensities.<sup>22</sup> The similar radiative lifetime is also supported by the discussion in Fig. 5c on the similar broadening in the single electron-hole pair transition of EHP and the transition of excitons. Third, the calculated charge densities for the onset and termination of EMT are consistent with theoretical prediction. Theoretically, EMT is expected to start when the Debye-Hückel screening length  $L_s$  is comparable to the Bohr radius  $a$ .<sup>22,43</sup> For monolayer MoS<sub>2</sub>, the critical charge density to enable EMT is predicted to be  $0.94 \times 10^{12} \text{ cm}^{-2}$  (see S3 for details).

Additionally, the gas-liquid phase transition is expected to occur when the chemical potentials of EHP and EHL are equal. Theoretical analysis of the chemical potential of electron-hole systems in monolayer MoS<sub>2</sub> predicts that the critical charge density of EHP to enable the gas-liquid phase is  $1.0 \times 10^{13} \text{ cm}^{-2}$  (see Ref.44 and also S4 for details)<sup>44</sup>. Both theoretical predictions reasonable match the calculation result in Fig. 3c.

### **Electron-Hole Plasma Bubbles**

In stark contrast with conventional wisdom, which believes the charge carriers in EHP are individually unbound, our experimental results indicate that the charge carriers in EHP exist in format of giant electron-hole complex in nanoscale size instead, which we refer as *EHP bubble*. This is evidenced by a distinct spatial distribution in the intensity and spectral features (peak position and spectral width) of the EHP emission. Without losing generality, we use the incidence power of 18.4 kW/cm<sup>2</sup> as an example. Figure 4a shows typical two-dimensional (2D) spatial-spectral images collected monolayer MoS<sub>2</sub>. The PL spectra extracted from different locations of the image and fitting results are plotted in Fig. 4b-d. While the intensity of the EHP emission substantially decreases with increase of the distance, the peak position and spectral width only shows minor variation. The similar peak position and spectral width in the EHP emission across the luminescence area is intuitively supported by the nice overlap of the low energy tails of all the PL spectra from different locations as shown in the top panel of Fig.4b. The low energy tail is expected to be dominated by EHP emission. In contrast, the PL spectra collected from the luminescence center under different incident powers show low energy tails well separated (bottom panel of Fig.4b) due to the substantial blueshift and narrowing of EHP emission (see Fig. 2d-f).

The distinct spatial distribution in the intensity and spectral features of the EHP emission is counter intuitive. The decrease in emission intensity suggests a substantial decrease in the charge

density with the distance increasing, but the minor change in the peak position and spectral width suggests only a mild distance-dependent variation in the charge density, as the peak position and spectral width of EHP emission are closely related with the charge density. This conflict can be conciliated by considering that the charge carriers in EHP exists in format of small clusters (referred as *EHP bubble*) rather than individual free charges as illustrated in Fig. 4e. The intensity of the EHP emission is collectively determined by the number density (number per unit area) of the bubbles and the charge density in each bubble, while the spectral width and peak position are only dictated by the charge density in each bubble. The experimental observation indicates that the number density of EHP bubbles decreases with the distance increasing, but the charge density in each bubble does not change much. Additionally, the similar charge density in all the EHP bubbles across the luminescence area indicates that the EHP bubbles are generated at the luminescence center and then diffuse outwards over the luminescence area.

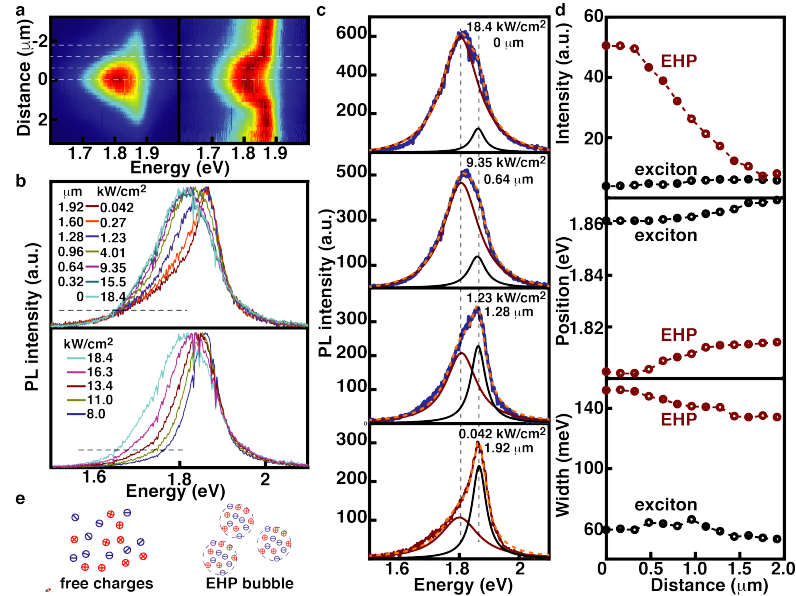


**Figure 4. Evidence for EHP bubbles.** (a) As-measured (left) and normalized (right) two-dimensional spectral-spatial PL image of monolayer MoS<sub>2</sub> collected at the incident power of 18.4  $\text{kW}/\text{cm}^2$ . In the normalized result, the PL spectrum at each position is normalized with respect to the local maximum intensity. Horizontal dashed lines indicate the location of the four

representative spectra given in (c). **(b)** Comparison of the PL spectra collect from different locations at 18.4 kW/cm<sup>2</sup> (top) and the PL spectra from the luminescence center at different incident powers (bottom). The legend in the top panel indicates the distance of each spectra away from the center and corresponding local incident power density. The dashed horizontal lines indicate the low energy tails of the spectra. **(c)** Measured and fitted PL spectra collected at different locations as indicated by the dashed horizontal lines in (a). The dashed lines connect the peak positions of the EHP and exciton emission. **(d)** Fitted intensity, position, and spectral width of the exciton emission (black) and EHP emission (red). **(e)** Schematic illustration for individual unbound charges and EHP bubbles.

These experimental results also indicate that EHP bubbles are stable. They can transport as a whole like free excitons and stably exist in environment with low exciton density, even the formation of the EHP bubbles requests a high density of excitons. This stability is rooted in the lower thermodynamic free energy of EHP bubbles than excitons. As discussed later in Fig.5, the position of the emission peak of EHP and excitons are dictated by free energy, and the lower energy emission peak of EHP bubbles (Fig. 4c) indicates a lower free energy. We believe it is the formation of stable EHP bubbles that differentiates the EMT and the entropy-driven ionization of excitons at low density,<sup>15,45,46</sup> the latter of which produces individual unbound electrons and holes that have free energy identical to excitons and bear no difference in emission from excitons.

We can roughly estimate the size of EHP bubbles on basis of diffusion coefficient as what reported previously.<sup>47</sup> According to the result in Fig. 4e, the diffusion length  $L_{\text{EHP}}$  of the EHP bubbles can be estimated to be around 1.2  $\mu\text{m}$ . We previously demonstrated that the lifetime  $\tau_{\text{EHP}}$  of EHP under comparable condition is around 100 ns.<sup>8</sup> Therefore, the diffusion coefficient  $D_{\text{EHP}}$  of the EHP bubble can be estimated to be around 0.15 cm<sup>2</sup>/s with  $D_{\text{EHP}} = L_{\text{EHP}}^2 / \tau_{\text{EHP}}$ . On the other hand, the diffusion coefficient of excitons is reported to be 22.5 cm<sup>2</sup>/s with the presence of EHP.<sup>35</sup> Because the diffusion coefficient is inversely proportional to the mass  $M$ , we can estimate the number of electron-hole pairs in the EHP bubble to be around 150. This corresponds to a size of around 50 nm at the charge density of  $0.88 \times 10^{13} \text{ cm}^{-2}$  at 18.4 kW/cm<sup>2</sup> that can be found at Fig. 3c.

This estimate matches our intuitive expectation. Since we can nicely resolve the space variation of the EHP emission intensity (top panel of Fig. 4e), the size of the EHP bubble must be smaller than the pixel of our CCD detectors, *i.e.* 160 nm. We expect the size and number of charges in EHP bubbles to vary with incident power, which would need more studies for better understanding.

### **Correlation of the emission spectral feature and charge density of EHP**

We also establish a quantitative correlation between the emission lineshape and charge density of EHP. It has been well accepted that the emission lineshape of EHP is associated with charge density. But previous studies all assumed that the emission profile of EHP is simple the convolution of the occupied electron and hole density of states at the conduction and valence bands, respectively.<sup>16,22</sup> This assumption works very well for the emission of EHL, but not for EHP, which has puzzled the community for decades.<sup>16,22</sup>

Instead, we find that EHP emission can be well fit with a Lorentzian oscillator as  $(\Gamma/2)^2/[(E-E_0)^2+(\Gamma/2)^2]$  (Fig. 2), where  $E_0$  is the peak position and  $\Gamma/2$  is a broadening term that dictates the FWHM  $\Gamma$  of the emission peak. The broadening of the EHP emission  $(\Gamma/2)_{\text{EHP}}$  is reasonably equal to a sum of the broadening of the exciton emission  $(\Gamma/2)_{\text{ex}}$  and the Fermi energy of the EHP. Fig. 5b plots the measured difference in spectral width between the EHP emission and the exciton emission  $(\Gamma/2)_{\text{EHP}} - (\Gamma/2)_{\text{ex}}$  (extracted from Fig. 2f). Also plotted is the Fermi energy of the EHP calculated on basis of the calculated charge density of EHP given in Fig. 3c (see the caption of Fig. 5 and S4 for more details). The calculation shows reasonable consistence with the experimental result. Additionally, the peak position  $E_0$  is determined by the electronic bandgap  $E_{\text{eBG}}$  of monolayer MoS<sub>2</sub> and EHP's free energy  $F_{\text{EHP}}$  as illustrated in Fig. 5a,  $E_0 = E_{\text{eBG}} + F_{\text{EHP}}$  ( see S4 for details of the calculation of free energy). Fig.5c shows the measured and calculated peak position  $E_0$  of the EHP emission. The calculation reasonably reproduces the measured peak

position and its trend of redshifting with the incident power increasing, except when the incident power is relatively low. The non-trivial deviation at low charge densities is rooted in the model we used for the calculation of free energy ( see S4 for details of the model), which involves the calculation of entropy on basis of statistic thermodynamics that might not work perfectly when the charge density is relatively low.

The correlation of the peak position and spectral width with the free energy and Fermi energy provides useful insight into EHP. As illustrated in Fig. 5c inset, the EHP bubble can be intuitively considered as a giant multi-excitonic specie with the transition occurring at the energy level defined by the free energy of the EHP. The transition of single electron-hole pairs in the EHP bubble has a broadening similar to that of the co-existing exciton transition  $(\Gamma/2)_{\text{ex}}$ . The large number of charges in EHP bubbles, which occupy multiple energy levels, increases the uncertainty in the transition energy and provides additional broadening in the emission spectra. The similar broadening in the single electron-hole pair transition of EHP and the transition of co-existing exciton also supports their similar radiative lifetime as suggested by the result in Fig. 3d.

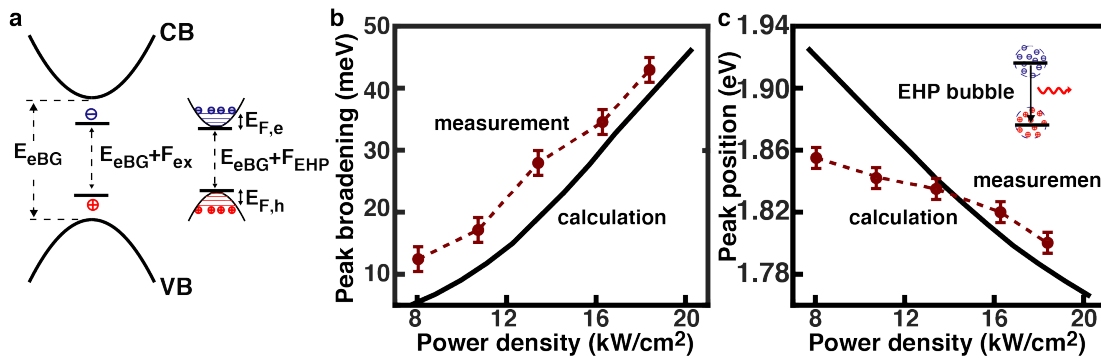


**Figure 5. Physics of EHP emission.** (a) Schematic illustration for the free energy and Fermi energy of EHP as well as its correlation with the emission peak position. The correlation between the peak position and the free energy of excitons (which is equal to the exciton binding energy) is also illustrated.  $E_{\text{eBG}}$  indicates the electronic bandgap of monolayer MoS<sub>2</sub>, which is 2.31 eV as judged from the exciton peak position ((1.89 eV) at low incident power and exciton binding energy (0.42 eV)<sup>40,48</sup>. The Fermi energy  $E_{\text{F,e}} = n_p \pi \hbar^2 / 2m_e$ ,  $E_{\text{F,h}} = n_p \pi \hbar^2 / 2m_h$ <sup>24</sup>, where  $\hbar$  is Planck's

constant,  $n_p$  is the density of unbound electron-hole pairs, and  $m_e$  and  $m_h$  are the effective mass of electrons and holes, respectively, see S4 for more details. **(b)** The calculated Fermi energy of EHP (black) and the measured difference in the broadening (half of the spectral width) of EHP emission and exciton emission (red) as a function of incident power. **(c)** The calculated (black) and the measured (red) peak position of EHP emission as a function of incident power. The calculated peak position is equal to the sum of the electronic bandgap (2.31 eV) and EHP's free energy ( $E_{\text{eBG}} + F_{\text{EHP}}$ , the free energy is negative). Inset, schematic illustration for the emission of EHP bubble.

## Conclusion

In conclusion, we have established a new physics scheme for the fundamentals of EMT by taking advantage of the extraordinary binding energy and atomically thin dimension of monolayer MoS<sub>2</sub>. The result addresses multiple long-standing controversies or puzzling issues, such as demonstrating the EMT is a continuous process, elucidating the criteria for the onset and termination of EMT, quantifying the equilibrium distribution of charge carriers in EHP and co-existing excitons, and clarifying the correlation between the emission profile and charge density of EHP. Additionally, the result defies the conventional wisdom and demonstrates that the charges in EHP exists as stable giant multi-excitonic species that may involve  $\sim 150$  electron-hole pairs and are in size of around 50 nm. Whereas we focus on monolayer MoS<sub>2</sub>, the new fundamental understanding is applicable to other 2D semiconductors and conventional semiconductor materials. The result lays down a foundation to use EMT in quantum science and to development devices with broad implication in lasers, LEDs, imaging sensors, and optical interconnects.

## Methods

*Synthesis and transfer of monolayer MoS<sub>2</sub>*: The monolayer was grown on SiO<sub>2</sub>/Si substrates using a chemical vapor deposition process,<sup>49</sup> and then was transferred onto the quartz substrates with pre-patterned holes in size of 4 $\mu$ m using a surface-energy-assisted transfer approach.<sup>50</sup> The holes were fabricated using standard photolithography and dry etching processes. In a typical transfer



process, 9 g of polystyrene (PS, MW=280 kg/mol) was dissolved in 100 mL of toluene. The PS solution was spin-coated (3000 rpm for 60 s) on the as-grown monolayer. This was followed with 85° C baking for 1 hr. A water droplet was then dropped to assist the lift off of the PS-monolayer assembly. The polymer-monolayer assembly was then transferred to the quartz substrate. The sample was baked for 30 minutes at 150° C. The PS was removed by rinsing with toluene and followed by bake at 80° C for 30 minutes.

*PL measurement:* PL measurements were performed using a focused 532 nm laser in radius of 1.10 $\mu$ m. PL was collected by a long distance 50 $\times$  objective and imaged through a long-pass filter with laser reflection light filtered out onto the entrance slit of a spectrometer. The spectrometer output was recorded with a PIXIS CCD camera. The PL imaging was recorded by moving the grating to the 0<sup>th</sup> order mode. In this collection mode, the spatial PL intensity distribution will be imaged onto the CCD camera at once. The PL spectrum was recorded by moving the grating to the 1<sup>st</sup> order diffraction mode. All the PL measurements were done with the samples placed in a chamber flown with Ar gas.

### **Supplementary Materials:**

Figures S1-S3

S1. Calculation of the steady-state exciton density

S2. Calculation of the charge density in EHP with Saha equation

S3. Calculation of the critical charge density for the onset of EMT

S4. Calculation of Fermi energy and free energy of charge carriers

### **Acknowledgments**

This work was supported by the National Science Foundation under a grant of EFMA 1741693.

### Author contributions

Y. Y. and L.C. conceived the idea, Y. Y. performed the measurement, Y. Y. and L.C. designed the experiments, analyzed the data and wrote the manuscript. and analyzed the data. G. L. helped with the synthesis and transfer of the samples. All the authors were involved in reviewing the manuscript.

### Competing financial interests

The authors declare no competing financial interests.

### References

1. Tinkham, M. *Introduction to Superconductivity*, (Dova Publication Inc., Mineola, New York).
2. Griffin, A., Snoke, D.W. & Stringari, S. (eds.). *Bose Einstein Condensation*, (Cambridge University Press, New York, 1996).
3. Mott, N.F. Metal-Insulator Transition. *Rev Mod Phys* **40**, 677-& (1968).
4. Horodecki, R., Horodecki, P., Horodecki, M. & Horodecki, K. Quantum entanglement. *Rev. Mod. Phys.* **81**, 865 (2009).
5. O'Brien, J.L. Optical Quantum Computing. *Science* **318**, 1567-1570 (2007).
6. Byrnes, T., Kim, N.Y. & Yamamoto, Y. Exciton–polariton condensates. *Nat. Phys.* **10**, 803-813 (2014).
7. Kasprzak, J., *et al.* Bose–Einstein condensation of exciton polaritons. *Nature* **443**, 409-414 (2006).
8. Bataller, A.W., *et al.* Dense Electron–Hole Plasma Formation and Ultralong Charge Lifetime in Monolayer MoS<sub>2</sub> via Material Tuning. *Nano Letters* **19**, 1104-1111 (2019).
9. Keldysh, L.V. & Lebedev, P.N. The electron-hole liquid in semiconductors. *Contemp. Phys.* **27**, 395 (1986).
10. Almand-Hunter, A.E., *et al.* Quantum droplets of electrons and holes. *Nature* **506**, 471-475 (2014).
11. Yu, Y., *et al.* Room-Temperature Electron-Hole Liquid in Monolayer MoS<sub>2</sub> *Acs Nano* **13**, 10351-10358 (2019).
12. Kogar, A., *et al.* Signatures of exciton condensation in a transition metal dichalcogenide. *Science* **358**, 1314-1317 (2017).

13. Wang, Z., *et al.* Evidence of high-temperature exciton condensation in two-dimensional atomic double layers. *Nature* **574**, 76-80 (2019).
14. Kappei, L., Szczytko, J., Morier-Genoud, F. & Deveaud, B. Direct Observation of the Mott Transition in an Optically Excited Semiconductor Quantum Well. *Phys. Rev. Lett.* **94** 147403 (2005).
15. A. Steinhoff, M.F., M. Rösner, G. Schönhoff, T.O. Wehling, F. Jahnke. Exciton fission in monolayer transition metal dichalcogenide semiconductors. *Nat. Commun.* **8**, 1166 (2018).
16. Shah, J., Combescot, M. & Dayem, A.H. Investigation of Exciton-Plasma Mott Transition in Si. *Physical Review Letters* **38**, 1497-1500 (1977).
17. E. J. Sie, A.S., C. Gies, C. H. Lui, Q. Ma, M. Rösner, G. Schönhoff, F. Jahnke, & T. O. Wehling, Y.-H.L., J. Kong, P. Jarillo-Herrero, and N. Gedik. Observation of exciton redshift-blueshift crossover in monolayer WS<sub>2</sub>. *Nano Lett.* **17**, 4210-4216 (2017).
18. Wang, J., *et al.* Optical generation of high carrier densities in 2D semiconductor heterobilayers. *Sci. Adv.* **5**, eaax0145 (2019).
19. Stern, M., Umansky, V. & Bar-Joseph, I. Exciton Liquid in Coupled Quantum Wells. *Science* **343**, 55-57 (2014).
20. Trevor B. Arp, D.P., Vivek Aji & Nathaniel M. Gabor. Electron-hole liquid in a van der Waals heterostructure photocell at room temperature. *Nat. Photon.* **13**, 245-250 (2019).
21. Simon, A.H., Kirch, S.J. & Wolfe, J.P. Excitonic phase diagram in unstressed Ge. *Phys. Rev. B* **46**, 10098 (1992).
22. Smith, L.M. & Wolfe, J.P. Time-Resolved Study of Electron-Hole Plasmas near the Liquid-Gas Critical-Point in Si - Evidence for a 2nd Condensed-Phase. *Physical Review B* **51**, 7521-7543 (1995).
23. You, Y.M., *et al.* Observation of biexcitons in monolayer WSe<sub>2</sub>. *Nat Phys* **11**, 477-U138 (2015).
24. Mak, K.F., *et al.* Tightly bound trions in monolayer MoS<sub>2</sub>. *Nat Mater* **12**, 207-211 (2013).
25. Lee, H.S., Kim, M.S., Kim, H. & Lee, Y.H. Identifying multiexcitons in MoS<sub>2</sub> monolayers at room temperature. *Phys. Rev. B* **93**, 140409(R) (2016).
26. Mak, K.F., Lee, C., Hone, J., Shan, J. & Heinz, T.F. Atomically Thin MoS<sub>2</sub>: A New Direct-Gap Semiconductor. *Physical Review Letters* **105**(2010).
27. Splendiani, A., *et al.* Emerging Photoluminescence in Monolayer MoS<sub>2</sub>. *Nano Lett.* **10**, 1271-1275 (2010).
28. Yu, Y., Minhaj, T., Huang, L., Yu, Y. & Cao, L. In-Plane and Interfacial Thermal Conduction of Two-Dimensional Transition-Metal Dichalcogenides. *Phys. Rev. Applied* **13**, 034059 (2020).
29. Chernikov, A., Ruppert, C., Hill, H.M., Rigosi, A.F. & Heinz, T.F. Population inversion and giant bandgap renormalization in atomically thin WS<sub>2</sub> layers. *Nat Photonics* **9**, 466-U469 (2015).
30. Qiu, Z., *et al.* Giant gate-tunable bandgap renormalization and excitonic effects in a 2D semiconductor. *Sci. Adv.* **5**, eaaw2347 (2019).
31. Fehrenbach, G.W., Schafer, W., Treusch, J. & Ulbrich, R.G. Transient Optical Spectra of a Dense Exciton Gas in a Direct-Gap Semiconductor. *Phys. Rev. Lett.* **49**, 1281-1284 (1982).

32. Liang, Y. & Yang, L. Carrier Plasmon Induced Nonlinear Band Gap Renormalization in Two-Dimensional Semiconductors. *Phys. Rev. Lett.* **114**, 063001 (2015).
33. Pogna, E.A.A., *et al.* Photo-Induced Bandgap Renormalization Governs the Ultrafast Response of Single-Layer MoS<sub>2</sub>. *Acs Nano* **10**, 1182-1186 (2016).
34. Cunningham, P.D., Hanbicki, A.T., McCreary, K.M. & Jonker, B.T. Photoinduced Bandgap Renormalization and Exciton Binding Energy Reduction in WS<sub>2</sub>. *Acs Nano* **11**, 12601-12608 (2017).
35. Yu, Y., Yu, Y., Li, G. & Cao, L. Giant Enhancement of Exciton Diffusivity in Two-Dimensional Semiconductors *submitted* (2020).
36. Yu, Y., *et al.* Fundamental limits of exciton-exciton annihilation for light emission in transition metal dichalcogenide monolayers. *Phys. Rev. B* **93**, 201111(R) (2016).
37. Amo, A., Martín, M.D., Viña, L., Toropov, A.I. & Zhuravlev, K.S. Interplay of exciton and electron-hole plasma recombination on the photoluminescence dynamics in bulk GaAs. *Phys. Rev. B* **73**, 035205 (2006).
38. Steinleitner, P., *et al.* Direct Observation of Ultrafast Exciton Formation in a Monolayer of WSe<sub>2</sub>. *Nano Lett.* **17**, 1455–1460 (2017).
39. Suzuki, T. & Shimano, R. Time-Resolved Formation of Excitons and Electron-Hole Droplets in Si Studied Using Terahertz Spectroscopy. *Phys. Rev. Lett.* **103**, 057401 (2009).
40. Yu, Y., Li, G. & Cao, L. Room Temperature Ballistic Exciton Transport in Two-Dimensional Semiconductors. *submitted* (2020).
41. Ebeling, W., Kraeft, W.-D. & Kremp, D. *Theory of Bound States and Ionization Equilibrium in Plasmas and Solids*, (Akademie-Verlag, Berlin, 1976).
42. Yariv, A. Coupled-Mode Theory for Guided-Wave Optics *IEEE J. Quantum Electron.* **9**, 919-933 (1973).
43. Rogers, F.J., H. C. Graboske, J. & Harmood, D.J. Bound Eigenstates of the Static Screened Coulomb Potential\*. *Phys. Rev. A* **1**, 1577-1586 (1970).
44. Yu, Y., Li, G. & Cao, L. Electron-Hole Nano-Droplet and Exciton Phase Diagram in Two-Dimensional Semiconductors *submitted* (2020).
45. Mock, J.B., Thomas, G.A. & Combescot, M. Entropy Ionization of an Exciton Gas. *Solid State Comm.* **25**, 279-282 (1978).
46. Koch, S.W., Kira, M., Khitrova, G. & Gibbs, H.M. Semiconductor excitons in new light. *Nat. Mater.* **5**, 523-531 (2006).
47. Pokrovskii, Y. Condensation of non-equilibrium charge carriers in semiconductors. *Phys. Stat. Sol.* **11**, 385 (1972).
48. Yu, Y., *et al.* Exciton-dominated Dielectric Function of Atomically Thin MoS<sub>2</sub> Films. *Scientific Reports* **5**, 16996 (2015).
49. Yu, Y., *et al.* Equally Efficient Interlayer Exciton Relaxation and Improved Absorption in Epitaxial and Nonepitaxial MoS<sub>2</sub>/WS<sub>2</sub> Heterostructures. *Nano Lett.* **15**, 486 (2014).
50. Gurarslan, A., *et al.* Surface-Energy-Assisted Perfect Transfer of Centimeter-Scale Monolayer and Few-Layer MoS<sub>2</sub> Films onto Arbitrary Substrates. *Acs Nano* **8**, 11522-11528 (2014).